Altered oscillatory coupling reflects possible inhibitory interneuron dysfunction in Rett syndrome

Devorah Kranz,[1,2] Yael Braverman,[1] Michelle McCarthy,[3] Claire Mackay, Karen Sabol,[1] Tim A. Benke, David Lieberman,[1,2] Eric D. Marsh,[4] Jeffrey L Neul,[5] Fleming Peck,[6] Alan K Percy,[7] Joni Saby,[4] Nancy Kopell,[3] Charles A. Nelson,[1,2] April R Levin,*[1,2] Michela Fagiolini*[1,2]

*Co-last authors

Abstract

Background Rett syndrome is a rare neurodevelopmental disorder caused primarily by pathogenic variants in the *MECP2* gene, leading to lifelong cognitive impairments. To understand the broad neural disruptions in Rett syndrome, it is essential to examine large-scale brain dynamics at the level of neural oscillations. Phase-amplitude coupling—a form of cross-frequency interaction that supports information integration across temporal and spatial scales—is a promising candidate measure for capturing such widespread neural dysfunction. Phase-amplitude coupling depends on the coordinated activity of specific neuronal subtypes, and while multiple subtypes are implicated in different aspects of the Rett syndrome phenotype, their role in shaping large-scale oscillatory dynamics in Rett syndrome is not well understood. To investigate this, we utilized a multi-level approach, combining EEG recordings with computational modeling to identify alterations in phase-amplitude coupling in Rett syndrome and probe their underlying cellular and circuit-level mechanisms.

Methods We recorded resting-state EEG from 38 individuals with Rett syndrome and 30 age- and sex-matched typically developing individuals. Phase-amplitude coupling was quantified: modulation index was obtained to determine coupling strength, and phase bias was assessed to examine the preferred phase of coupling. We characterized phase-amplitude coupling across all low and high frequency combinations and electrodes, as well as within canonical theta-gamma and alpha-gamma frequency pairs across four predefined cortical regions. Finally, we modeled a biophysically-constrained Layer 4 cortical network to propose a possible mechanism underlying changes to oscillatory dynamics.

Results We found significantly stronger phase-amplitude coupling in Rett syndrome across widespread cortical regions and frequency pairs, with a pronounced increase in theta-gamma and alpha-gamma coupling in anterior, posterior, and whole-brain regions ($P < 0.05$). Individuals with Rett syndrome also exhibited a more positive alpha-gamma phase bias in anterior and whole-brain regions ($P < 0.05$). Biophysically constrained modelling demonstrated that reduced VIP-expressing interneuron activity alone could recapitulate the pattern of increased theta-gamma and alpha-gamma phase-amplitude coupling observed in Rett syndrome ($P < 0.001$).

Conclusions These findings identify alterations in awake-state phase-amplitude coupling in Rett syndrome and propose a mechanistic link to VIP+ interneuron dysfunction. Elevated phase-amplitude coupling may serve as a promising biomarker of cortical dysfunction and a

translational bridge from neural circuitry to clinically observable EEG signatures. By implicating VIP+ interneurons, our results open new avenues for testing interventions in preclinical models to identify potential novel therapeutic targets for individuals with Rett syndrome.

Author Affiliations

1. Boston Children's Hospital, Boston, MA 02115
2. Harvard Medical School, Boston, MA 02115
3. Boston University, Boston MA 02215
4. Departments of Neurology and Pediatrics, University of Pennsylvania Perelman School of Medicine and Children's Hospital of Philadelphia, Philadelphia PA 19096
5. Department of Pediatrics, Vanderbilt University Medical Center, Nashville TN 37203
6. Department of Psychology, University of California Los Angeles
7. University of Alabama, Heersink School of Medicine, Department of Pediatrics (Neurology)

Correspondence to:
Dr. Michela Fagiolini, michela.fagiolini@childrens.harvard.edu, Center for Life Sciences, 3 Blackfan St, Boston, MA 02115
Dr. April Levin, april.levin@childrens.harvard.edu, 2 Brookline Place, BCH 3433, Brookline, MA 02445

Keywords

Rett syndrome; neurogenetic disorders; EEG; phase-amplitude coupling; VIP+ interneurons

Introduction

Rett syndrome (RTT) is a rare X-linked neurodevelopmental disorder that presents with an initial period of typical development followed by rapid regression resulting in profound cognitive, motor, and autonomic impairments including loss of purposeful hand use and spoken language.[1,2] The majority of RTT cases are caused by de novo pathogenic variants in the X-linked *MECP2* gene, which encodes methyl-CpG-binding protein 2 (MeCP2).[3] Although MeCP2 is expressed widely throughout the body, its levels are 5 to 10-fold higher in neurons compared to other cell types, and neuronal dysfunction is central to RTT pathology.[4] MeCP2 influences the brain's cellular and network development across the lifespan: its function affects prenatal neurogenesis, development of neuronal circuitry, and maintenance of adult neural function.[5–8] Given these widespread alterations across diverse brain regions and functions, understanding RTT pathophysiology requires investigating neural dynamics at the level of large-scale brain networks.[1,9]

Brain-wide dynamics rely heavily on coordination of and by neural oscillations—rhythmic patterns of neuronal activity characterized by frequency, amplitude, and phase—that facilitate communication between distant cortical regions and support cognitive processing.[10] Electroencephalography (EEG) provides a valuable non-invasive and clinically relevant tool to

assess these oscillations and is particularly suitable for use in RTT populations as it can be recorded without requiring active task engagement. Clinical EEG in RTT has long revealed visually observed abnormalities such as epileptiform discharges and diffuse slowing of activity that persists into adulthood.[11–13] Recent quantitative studies have expanded upon these findings, revealing evidence of region-specific disturbances to spectral power (which examines the power of each individual frequency present in the signal), including increases in delta (1-3 Hz) and theta power (4-7 Hz), reductions in alpha power (8-12 Hz), and alterations in the 1/f spectral slope.[14,15] While spectral power analyses offer insight into the overall magnitude of neural oscillations, they provide limited information about how these oscillations dynamically interact to support cognitive processes, or how circuit-level dysfunction in RTT can disrupt communication between brain regions or alter precise timing mechanisms essential for cognition.

Phase-amplitude coupling (PAC), which evaluates how the phase of low-frequency oscillations modulates the amplitude of high-frequency activity, has been proposed as a fundamental mechanism of neural coordination across spatial and temporal scales.[16–18] PAC has been observed in diverse electrophysiological signals, from intracellular recordings to scalp EEG, highlighting its relevance across different levels of neural activity. It is thought that PAC serves as a clocking mechanism, generating temporal windows that allow for the integration of relevant information.[19] Notably, PAC strength and phase bias—the phase of the slow wave at which coupling occurs—can vary by cortical layer and are influenced by interneuron function.[20–22]

PAC between canonical frequency pairs is particularly relevant to specific domains of brain function and has been shown to be functionally important to a range of core cognitive processes. Theta-gamma coupling is implicated in working memory, with theta phase modulating gamma amplitude to organize memory encoding and retrieval in the hippocampus and prefrontal cortex.[23–26] Alpha-gamma coupling, meanwhile, has been linked to computations in visual cortical areas, where alpha phase modulates local gamma activity, facilitating selective attention, visual information integration, and prioritization of sensory input based on stimulus saliency.[27] Altered PAC has been reported in autism spectrum disorder (ASD) and other neurogenetic disorders, both in resting-state EEG[26] and during specific cognitive tasks.[29–33] In RTT, abnormal PAC has recently been identified during slow-wave sleep,[34] but its presence during the awake state—particularly at faster frequency pairs associated with memory and attention—has not yet been studied. Moreover, precisely which neuronal subpopulations and circuit mechanisms drive RTT-related oscillatory abnormalities remains an area of active investigation.

In *Mecp2* mutant mice, which replicate key aspects of the RTT phenotype, cortical circuit dysfunction is characterized by an imbalance in excitatory-inhibitory signaling[35–37], and studies employing techniques such as selective deletion of *Mecp2* from specific neuronal subtypes have clarified how distinct cell populations individually contribute to these network disruptions.[38–40] Pyramidal (PYR) neuron activity is significantly reduced, particularly in sensory cortical regions, leading to progressive silencing of visual circuits and decreased visual acuity.[35,37,41] Alterations in GABAergic interneurons have also been strongly implicated[42]: parvalbumin-positive interneurons (PV+INs), which normally provide fast-spiking inhibition to PYR neurons, exhibit increased connectivity and activity in *Mecp2* mutant mice.[36] Vasoactive intestinal peptide-expressing interneurons (VIP+INs) in particular have emerged as especially relevant to circuit and oscillatory dysfunction. VIP+INs synapse onto both PYR cells and other interneurons,[43,44]

modulating sensory gain[45–49] and driving oscillatory activity.[50,51] Early disruptions in VIP+IN activity broadly compromise cortical circuits, resulting in weakened synaptic inhibition, impaired experience-dependent plasticity, and abnormal cortical maturation.[45] Deficits in VIP+IN excitability and modulation have been reported in mouse models of other neurodevelopmental disorders[52,53] that share some clinical features with RTT.[54,55] Notably, recent studies demonstrate that selective deletion of *Mecp2* from VIP+INs alters their intrinsic activity and recapitulates core phenotypic features of RTT[40], positioning VIP+IN dysfunction as a compelling avenue for understanding altered cortical dynamics in RTT.

In the present study, we adopted a multi-level approach, characterizing neural dynamics from both top-down and bottom-up perspectives. We first investigated phase-amplitude coupling patterns during awake resting state EEG in individuals with RTT. Since the specific frequencies and cortical regions where PAC may be disrupted in RTT are currently unknown, we initially conducted a data-driven analysis examining coupling comprehensively across all possible frequencies and brain regions. Subsequently, we focused our analyses on two canonical frequency pairs—theta-gamma and alpha-gamma—given their established roles in cognitive processing, and to allow for more detailed assessments of the distribution of PAC across each group. We identified abnormal PAC in individuals with RTT compared to typically developing controls, revealing significantly elevated coupling across multiple frequency bands and cortical regions, particularly in the alpha-gamma and theta-gamma ranges.

To identify potential neuronal and network mechanisms underlying the increased theta-gamma and alpha-gamma coupling seen in RTT, we then took a bottom-up approach by constructing a biophysically-constrained network model of cortical Layer 4 (L4) comprising pyramidal neurons and three key inhibitory interneuron classes: somatostatin (SOM+), PV+, and VIP+ interneurons. We focused our investigation on L4 for three reasons: (1) a major source of cortical alpha is thought to come via thalamocortical interactions which include L4[20,56]; (2) increased theta-gamma coupling has been associated with thalamocortical dysfunction[57]; (3) interneurons are key mediators of oscillatory brain activity[58–60] and L4 consists of a relatively large 7/1 ratio of inhibitory to excitatory neuronal subtypes.[61] Of note, biophysically-constrained models have been instrumental in revealing the connection of interneuron activity to rhythmic network dynamics.[62–64] Here, our computational model suggests that decreased excitability of VIP+ interneurons alone could account for the observed PAC alterations in L4 dynamics.

By integrating clinical EEG findings with mechanistic insights from animal models and computational modeling, our approach provides a unique translational framework for linking electrophysiological biomarkers with underlying cellular and circuit-level disruptions in RTT. Establishing PAC as a quantitative marker of cortical dysfunction could enable more precise tracking of disease progression and facilitate the evaluation of therapeutic interventions, and importantly, our findings open new potential pathways to test in preclinical models in order to identify potential novel therapeutic targets in individuals with RTT.

Materials and Methods

Participants

Participants were enrolled in one of two studies whose data were combined for the analyses presented here:

1. Natural History Study of Rett and Related Disorders (NHS) (U54 HD061222; NCT02738281).[65] Data were acquired across three study locations (Boston Children's Hospital (BCH), Vanderbilt University Medical Center (VUMC), or Children's Hospital Colorado (CHCO). The experimental protocol was approved and overseen by the Institutional Review Boards at each site.
2. IDDRC Rett Syndrome Biomarkers Study (RSBS). Data were acquired only at BCH. The experimental protocol was approved and overseen by the Institutional Review Board at Boston Children's Hospital.

Table 1 Participant Information

	Diagnostic Group	
	RTT (*n* = 38)	**TD (*n* = 30)**
Clinical Severity Score		
<10	5	
10->19	15	
20->29	13	
30->39	3	
Rett Diagnosis		
Typical	29	
Atypical	9	
Seizures		
None (with or without meds)	28	
Monthly	1	
Weekly	5	
Daily	1	
Sex		
Female	35	28
Male	3	2
Age	Range: 1-45	Range: 1-15
	Median: 8.5	Median: 6.0
	IQR: 11.75	IQR: 6.0
Usable EEG		
Yes	38	30
No	13	0
Collection Site		
VUMC	11	1
BCH	26	25
CHCO	1	4
Study		
RSBS	23	19
NHS	15	11

Participants were 1-46-year-old individuals with Rett Syndrome (RTT; n = 51) and typical development (TD; n = 30). While many prior studies in RTT have focused on a narrower age range, we chose this wider range to capture the full spectrum of the disorder, and examined the effects of age on our analyses as described below. Participants were recruited through hospital-

based Rett clinics, a research registry, clinical referrals, community sources, and word of mouth. Informed consent was obtained from all guardians or participants above 18 years old, and assent from all participants developmentally able.

In the RTT group, inclusion criteria included being 12 months to 50 years old at time of enrollment and a diagnosis of RTT with a previously identified pathogenic or likely pathogenic variant in the *MECP2* gene. TD participants were recruited to be approximately age and sex-matched to the RTT participants and were included if they had no underlying genetic diagnoses or prior medical conditions associated with increased likelihood of ASD or intellectual disability. In both groups, the primary language of participants and caregivers was English. Exclusion criteria for the RTT group included taking an investigational drug as part of another research study within 30 days prior to study enrollment.

Demographic and other characteristics are reported in Table 1.

EEG data collection

Participants in the RSBS study watched an approximately five-minute video consisting of repeating silent videos akin to screensavers which directed their attention to the monitor. Each video played forward for 15 seconds and then in reverse for 15 seconds and video display was limited to 7 x 9.3 cm to minimize eye movement during task completion. The procedure for the NHS study differed slightly, in that participants watched a silent video of their choice. A behavioral assistant sat in the room with the participant to keep them as calm as possible.

Continuous EEG data were recorded at "rest" (i.e., with no time-locked stimuli), during the awake quiet state in dim lighting via a Net Amps 400 amplifier using the 128-channel Hydrocel Geodesic Net (Electrical Geodesic, Inc., Eugene, OR) with a sampling rate of 1000 Hz.

EEG data pre-processing

EEG data preprocessing was conducted using the Batch EEG Automated Processing Platform (BEAPP).[66] Within BEAPP, data were artifact detected and corrected using the Harvard Automated Processing Pipeline for Electroencephalography (HAPPE) 1.0, a pipeline optimized for EEG data collected from young children with neurodevelopmental disorders.[67] Data were first bandpass filtered using a high pass (1 Hz) and low pass (100 Hz) filter and resampled to 250 Hz. Only the 18 electrodes in the international 10–20 system were chosen for further processing and analysis. HAPPE applied line noise removal at 60 Hz via CleanLine's multi-taper method and then automatically detected and rejected bad channels, movement, muscle, and eye blink artifact with wavelet-enhanced independent component analysis (ICA) and ICA with Multiple Artifact Rejection Algorithm (MARA).[68,69] Following artifact removal, bad channels were interpolated using spherical interpolation and data were re-referenced to an average reference. Data were then segmented into overlapping 6 second segments (20% overlap), and a 2-second buffer was included at the beginning and end of each EEG segment to avoid edge effects from filters. (In other words, the buffer resulted in 10-second segments, but only the middle 6 seconds were analyzed). Segments were rejected based on HAPPE's recommended amplitude cut off

(40μV) and joint-probability rejection criteria. 55 randomly selected segments were chosen for each participant for subsequent analysis.

EEG rejection criteria

Participants were rejected if they had fewer than 55 EEG segments (330 seconds) of usable data or fell outside of 3 standard deviations from the mean on the following HAPPE quality control parameters: percent good channels, mean retained artifact probability, median retained artifact probability, percent of independent components rejected as artifact, and percent of EEG signal variance retained after artifact removal. Based on the above criteria 13 of the 81 EEGs collected were rejected (these were all from RTT participants, likely due to movement artifact) (Table 1).

Phase-amplitude coupling

As previously described in Mariscal[70] and Peck[28], the following PAC computations were computed using the *pactools* Python toolbox. For each segment, first narrowband neural oscillations at low (2-20 Hz in 2 Hz steps) and high (20-100 Hz in 4 Hz steps) frequencies were extracted. Low frequencies were filtered using a constant bandwidth of 2 Hz, while high frequencies were filtered using an upper sideband variable bandwidth, equal to the low frequency of interest.[71] Filtering at this step consisted of a zero-phase cosine-based filter to extract the real component and then a sine-based filter to extract the imaginary component, resulting in a complex-valued output signal.[72]

The low frequency phase and high frequency amplitude time series were obtained from the filtered signals. The phases of the low frequency signals were binned into 18 20-degree intervals (-180° to 180°), and the mean of the amplitude of the high frequency signals within each phase bin was calculated. The amplitude values were then normalized by dividing each bin average by the sum of all bin averages. The resulting phase-amplitude distributions were averaged across all 55 segments within participant to minimize noise.

After averaging the phase-amplitude distribution across segments, coupling strength, also known as the Modulation Index (MI*raw*), was computed as the Kulback-Leibler divergence of the phase-amplitude distribution from a uniform distribution (this is embedded in *pactools).*[73] To isolate the effect of PAC strength from related factors that may generate spurious phase-amplitude coupling (e.g. spectral power), phase amplitude distributions and coupling strength were also computed from a surrogate dataset that did not represent real effects of PAC. This surrogate dataset (MI*surr*) was generated by offsetting the high frequency and low frequency signals randomly from .1 to 1.9 seconds. The modulation index was computed for 200 different iterations of this surrogate, null phase-amplitude coupling data. Next, a normalized z-scored modulation index was computed using the surrogate distribution; this method was proposed in Dupré La Tour.[72] In carrying out these steps three measures were obtained from the original PAC strength: MI*raw*, MI*surr*, and MI*norm*, where MI*norm* is computed as the z-score of the MI*raw* compared to the distribution of MI*surr* values (previously termed z-MI in Mariscal[70]).

Phase-amplitude coupling strength: all frequencies and regions

To characterize diagnostic differences in patterns of PAC agnostic to canonical frequency bands, a data-driven approach was first employed, where analysis was performed across all frequency pairs and all channels.

To identify which frequency pairs and channels had statistically significant PAC within each group, a cluster-based approach was utilized, similar to Mariscal.[70] The following steps were repeated for the RTT and TD groups separately.

1. For each low and high frequency pair within every channel, a t-test was conducted to compare the MI*raw* values across all files within the group to the mean MI*surr* values across all files within the group.
2. "Frequency grouping" size was identified as the number of adjacent significant frequency pairs within a channel, excluding diagonals.

To determine the significance of these frequency grouping sizes, MI*raw* and MI*surr* were flipped in a randomly selected subset of half the participants ranging from 1 to half the sample, and the same test statistics and frequency grouping sizes were computed (steps 1 and 2 above). This process was repeated 1000 times to generate a null distribution of frequency grouping size. Finally, the original frequency grouping sizes that were larger than the 95th percentile of this null frequency grouping size distribution were determined to reflect significant PAC.

To determine differences in PAC strength (MI*norm*) between groups, a cluster-based approach was utilized again. The same analysis steps were conducted, now comparing MI*norm* from each group (rather than MI*raw* and MI*surr* from all files). In this analysis, t-tests were similarly conducted to compare MI*norm* between groups at each frequency pair, and frequency grouping sizes that exceeded the permutation-generated null frequency grouping size distribution were determined to reflect statistically significant differences in PAC strength between groups.

Phase-amplitude coupling strength: a-priori defined regions of interest and canonical wavebands

Next, a-priori defined regions of interest and canonical wavebands were examined. Group differences in PAC strength were evaluated using the modulation index averaged over all segments for each individual normalized by the surrogate distribution (MI*norm)*. PAC strength was calculated across four brain regions of interest: anterior (FP1, FP2, F3, F4, F7, F8, Fz), posterior (O1, O2, T5, T6, Pz), midline (C3, C4), and whole-brain (all 10-20 channels), and in the following frequency pairs: theta (4-7 Hz) and gamma (28-56 Hz) and alpha (8-12 Hz) and gamma (28-56 Hz). A series of independent samples t-tests were used to test whether any differences between groups were significant.

Phase bias analysis

While the MI value represents the overall strength of phase-amplitude coupling, phase bias (or phase preference) reflects whether the high-frequency amplitude is preferentially modulated during specific phases of the low-frequency oscillatory cycle. To compute phase bias, the amplitude of the high-frequency oscillation was averaged across 18 phase bins spanning one full low frequency cycle for each participant. For each frequency pair, phase bias was calculated as the proportion of the high frequency amplitude occurring in the positive phase range (0° to

+180°), divided by the total amplitude across all bins, and then centered by subtracting 0.5. This yielded a scalar value per participant per frequency pair, where:

- Positive values indicate greater high frequency amplitude during the *falling phase* of the low frequency oscillation,
- Negative values indicate greater amplitude during the *rising phase*,
- Values near zero indicate no consistent phase preference.

The low frequency phase was derived using a cosine-based filter, with 0° corresponding to the waveform peak, ±90° to the zero crossings (rising at –90°, falling at +90°), and ±180° to the trough. Group-level comparisons of phase bias were performed using Mann–Whitney U tests.

Phenotypic Assessments

Associations between PAC metrics in all canonical brain regions and frequency pairs and age as well as clinical severity were examined. Clinical severity was assessed by clinicians using the Clinical Severity Scale (CSS)[74] and Clinical Global Impressions of Severity (CGI- S).[75,76] For RSBS participants only, associations with several other phenotypic measurements were also evaluated using parent-reported questionnaires: Rett Syndrome Behavior Questionnaire (RSBQ),[77–79] Sensory Profile 2 (SP2),[80,81] Vineland Adaptive Behavior Scales,[82,83] and Anxiety Depression and Mood Scale (ADAMS).[84,85] Scores and questionnaires were obtained close to or on the same day as the EEG recording. Linear regression analyses were computed separately for the RTT and TD groups, and False Discovery Rate was used to correct for multiple comparisons and applied to p-values. MATLAB was used to run all statistical analyses.

Modeling PAC

We constructed a biophysical model of Layer 4 cortical networks using single-compartment neurons with Hodgkin-Huxley-type dynamics (Fig. 5). The network model included excitatory pyramidal neurons or stellate neurons (PYR) and inhibitory interneurons. The interneuron populations consisted of the three most common types of interneurons found in cortex: PV+INs, SOM+INs and 5HT3aR+INs.[86] We used the VIP+IN subtype of 5HT3aR+ INs in our model since we were particularly interested in how VIP+IN activity affects network dynamics—VIP+INs have been implicated in mediating Rett symptoms by specific deletion of MeCP2 in VIP+ cells.[40] The model VIP+INs had D-, M- and T-currents which allowed for bursts of spikes at a delta time scale. L4-targeting SOM+INs (also known as X94 SOM+ interneurons) have a unique electrophysiological profile among cortical SOM+ cells, which includes stuttering behavior at alpha frequency[40,87]. Our model L4 SOM+INs had D-, A- and h-type membrane currents that produced the alpha frequency stuttering. We note that rodent L4 differs in cell types and circuits depending on cortical area. Specifically, rodent S1—the cortical areas mediating the rodent's more specialized sense of somatosensation—includes X94 SOM+ cells, whereas rodent V1 does not. We chose the more specialized cortical area of rodent S1 to model human L4. The PV+INs and PYRs were modeled using previous formulations of these cell types.[88] Each cell type was connected to other types of neurons and to other cells of its own type with varying types, strengths and degrees of connectivity constrained by existing literature that we were familiar with (see Supplementary Methods for more details). The network consisted of 110 neurons, with the number of each cell type roughly proportional to their prevalence in cortex.[86] All neuronal subtypes were connected to each other through excitatory (AMPA) or inhibitory

(GABAa) synapses, with weights assigned according to available information. All neurons within the same class were connected to each by electrical and/or chemical synapses.

We studied the network activity under typical (baseline) and low VIP+IN activity levels, running 20 simulations for each condition. To decrease the activity of VIP+INs we lowered the maximal sodium current conductance of the VIP+INs by 22.5 mS/cm^2, which lowered the spiking rate of VIP+INs, but did not silence them. In simulations where specific types of interneurons were removed from the network, we sufficiently lowered either the maximal sodium conductance or the background excitation to those neurons such that spiking was eliminated in that neuronal subtype. We ran 7 simulations under each condition of removing one type of interneuron.

The local field potential (LFP), which is similar to the EEG in that it records extracellular voltage fluctuations but is different in that it is more spatially restricted than EEG, was modeled as the sum of all excitatory currents among PYR neurons in the network (as in Adam et al., 2024).[89] To compute phase-amplitude coupling we followed the methods in Kramer et al., 2016.[90] Phase amplitude coupling was determined by first bandpass filtering the model LFP at gamma, theta and alpha frequencies (where the ranges of all frequencies were the same as those used for the clinical EEG data) followed by extraction of phase and amplitude information of the low (theta and alpha) and high (gamma) frequencies, respectively using the Hilbert transform; this procedure generates phase and amplitude time-series vectors. We then computed the average amplitude of gamma for each phase of the low frequency oscillations and found the difference (h) between the maximum and minimum values of the average amplitude. To determine the statistical significance of h, we compared h to the difference between the maximum and minimum values of h produced from 1000 surrogate phase-amplitude vectors generated by randomly permuting the amplitude time series to assign each time point of the phase vector to a random amplitude. Significant phase-amplitude coupling was determined by calculating the p-value, which was computed as the proportion of h-values from the surrogate phase-amplitude data greater than the h-value from the non-randomized phase-amplitude data. The raw modulation index (MI) for each high and low frequency pair was calculated using the method described above (Kulback-Leibler divergence of the phase-amplitude distribution from a uniform distribution).[73] A two-sample t-test was used to evaluate for a significant difference between the mean of the MI values for simulations run under different conditions.

The code for the model was written in C++. Both the analysis of data and the graphics used MATLAB. All code will be made available on GitHub. See Supplemental Methods for more details.

Results

To investigate brain-wide oscillatory dynamics in RTT, we analyzed phase-amplitude coupling during resting awake-state EEG recorded from 38 individuals with a confirmed diagnosis of RTT and 30 typically developing participants. We obtained low frequency phase and high frequency amplitude time series from the EEG data and extracted phase-amplitude distributions, used throughout the following analyses (see Methods).

PAC in Rett syndrome and typical development across all possible frequencies and regions

We used a data-driven approach agnostic to pre-defined canonical frequency ranges to characterize any patterns in PAC that may not be captured otherwise, evaluating coupling between all possible frequency pairs and across all 18 electrodes.

Because PAC has not been previously described in the awake state in RTT, we first asked at what channels and at what frequency pairs significant PAC occurs. Using a cluster-based permutation analysis, we compared observed PAC to randomized data to identify regions and frequency pairs where coupling was significant. Figure 1 visualizes instances of significant coupling for RTT and TD independently, in a binary manner, agnostic to the strength of the coupling. We identified significant coupling in all electrodes for both groups with a high level of overlap (Fig. 1). Interestingly, in many electrodes (most strikingly F4, F8, T3, T4, C3, C4, and O1), the RTT group, but not the TD group, exhibited significant PAC in slower frequencies paired with gamma (Fig. 1).

[Insert Figure 1 here]

Figure 1. Instances of significant phase-amplitude coupling for RTT and TD independently across all possible frequencies and regions. Topoplot of comodulagrams visualizing significant PAC frequency pairs in RTT (n = 38) and TD (n = 30) for all 18 electrodes of the 10-20 channel array. Each subplot represents one electrode, and all subplots share the same axes of low and high frequency filtered signal, as shown in the lower left corner. Significant PAC frequency pairs are color-coded for RTT (red) and TD groups (blue), with any overlapping significant coupling shown in orange. On every subplot, each (x, y) coordinate with colored shading represents an instance of significant coupling between the corresponding low frequency (x) and high frequency (y) signals. Significance was calculated using a cluster-based permutation test.

To investigate the differences in PAC between RTT and TD in this data-driven approach, we next quantified the *strength* of coupling by calculating normalized modulation index, or MI, and averaging within each group. In Figure 2, RTT MI was subtracted from TD and plotted to visualize the difference in coupling strength between groups; regions and frequency pairs where differences were significant were identified using independent samples t-tests and indicated. We found that PAC was stronger in RTT compared to TD in a large portion of frequency pairs and electrodes, and that a portion of these differences in MI were statistically significant in every electrode ($P < .05$) (Fig. 2). Notably, slower frequencies paired with gamma appeared particularly stronger in RTT, and lower gamma was predominantly affected (Fig. 2).

[Insert Figure 2 here]

Figure 2. Difference between RTT and TD in phase-amplitude coupling strength across all possible frequencies and regions. Topoplot of comodulagrams visualizing PAC strength difference between RTT (n = 38) and TD (n = 30) for all 18 electrodes of the 10-20 channel array. Each subplot represents one electrode, and all subplots share the same axes of low and high frequency filtered signal, as shown in the lower left corner. On every subplot, each (x, y) coordinate represents RTT subtracted from TD strength of coupling between the corresponding low frequency x and high frequency y signal. Dark green shading corresponds to higher PAC strength in RTT than TD, whereas bright yellow shading corresponds to higher PAC strength in TD than RTT. Lighter green indicates areas of low PAC strength difference. White boundaries outline areas where coupling strength is significantly different between groups. Significance was calculated using independent sample t-tests with a threshold of .05.

PAC strength is increased in Rett syndrome in canonical theta-gamma and alpha-gamma frequency pairs

We next quantified coupling strength for each participant within the groups, focusing on four regions of interest (anterior, posterior, midline, and whole-brain) and the two canonical frequency pairs that have been most affected in other neurodevelopmental disorders (alpha-gamma and theta-gamma).[28,33,70,71] We found that RTT participants had significantly higher MI compared to TD in in the alpha-gamma frequency pair in anterior, posterior, and whole-brain regions, and in the theta-gamma frequency pair in posterior, midline, and whole-brain regions (independent samples t-test, $P < .05$) (Fig. 3). While a subset of participants in the RTT group showed MI values comparable to those in the TD group in each region, overall variability was greater across individuals, and PAC strength was markedly elevated in the RTT group in most regions we evaluated (Fig. 3).

[Insert Figure 3 here]
Figure 3. Theta-gamma and alpha-gamma PAC strength elevated in individuals with Rett syndrome. Markers in each subplot signify a single individual's normalized PAC strength for a given frequency pair and region (indicated on the top and left). TD participants (n = 30) are shaded in blue and RTT participants (n = 38) are shaded in red. Difference between groups was calculated using an independent samples t-test, where *** indicates $P < 0.001$, ** indicates $P < 0.01$, and * indicates $P < 0.05$. Group mean (horizontal lines) and standard error (vertical lines) are plotted.

PAC phase preference is more positive in the alpha-gamma frequency range in Rett syndrome

To further probe group differences in PAC, we examined at what point within the low-frequency cycle this coupling occurred, known as phase bias. Specifically, we computed phase bias using a metric that captures whether the high-frequency amplitude tended to occur preferentially during the rising or falling phases of the low frequency oscillation, where positive values reflect greater coupling during the falling phase (from peak to trough) and negative values indicate greater coupling during the rising phase (from trough to peak).

We focused on the same canonical frequency pairs and plotted individual alpha-gamma and theta-gamma phase bias across anterior, posterior, midline, and whole-brain regions. RTT participants exhibited significantly more positive alpha–gamma phase bias compared to TD in anterior and whole-brain regions (Mann-Whitney U test, $P < .05$) (Fig. 4A). Correspondingly, in RTT, gamma amplitude peaked slightly earlier in the alpha cycle compared to TD (Fig. 4B). We did not observe a significant group difference in alpha-gamma phase bias in the posterior region or in theta-gamma phase bias in any region.

[Insert Figure 4 here]
Figure 4. Alpha-gamma phase preference altered in Rett syndrome. TD participants (n = 30) are shaded in blue and RTT participants (n = 38) are shaded in red. **(A)** Markers in each subplot signify a single individual's theta-gamma or alpha-gamma phase bias values in four given regions. Difference between groups was calculated using a Mann-Whitney U test, where *** indicates $P < 0.001$, ** indicates $P < 0.01$, and * indicates $P < 0.05$. Group mean (horizontal lines) and standard error (vertical lines) are plotted. **(B)** Gamma amplitude plotted as a function of alpha phase in four given regions. Traces represent group averages, where amplitude means are plotted. Error bars represent standard deviation values. 0° corresponds to the peak of the low frequency, +90° corresponds to the falling phase of the low frequency, 180° or -180° corresponds to the trough of the low frequency, and -90° corresponds to the rising phase of the low frequency.

Phenotypic Assessments

Despite the robust group differences in PAC between RTT and TD participants, no associations between PAC metrics and clinical or phenotypic measures reached significance.

Modeling of Layer 4 network implicates VIP+IN dysfunction in increased theta-gamma and alpha-gamma PAC

To explore the underlying cellular and network mechanisms of changes to PAC in RTT, we constructed a biophysically constrained model of cortical Layer 4 containing excitatory neurons (PYR) as well as PV+, SOM+ and VIP+ interneurons (Fig. 5). Since VIP+INs have been implicated in mediating RTT symptoms,[40] we were particularly interested in whether deficiency in VIP+IN activity could account for the elevated PAC we observed in RTT. We therefore studied the model network activity under typical (baseline) and low VIP+IN activity levels.

[Insert Figure 5 here]
Figure 5. Schematic of L4 network. PYR represents excitatory stellate and/or pyramidal cells, PV represents fast spiking parvalbumin+ cells, SOM represents somatostatin+ cells projecting to L4, and VIP represents VIP+ cells. Each represents a population of cells of a given cell type. In isolation (without network connections), VIP+ cells produce delta/theta (2 – 4 Hz), SOM+ cells produce alpha, and the reciprocal interaction between PYR and PV+ cells produces gamma via PING (pyramidal cell – interneuron gamma). Noisy input is given to pyramidal cells to represent thalamic input and/or input from other cortical areas. Excitatory synaptic connections are represented by red arrows and inhibitory connections are represented by blue arrows.

At typical (baseline) levels of VIP+IN activity, networks showed significant participation of all neuronal subtypes (Fig. 6A, left). VIP+INs and SOM+INs were mutually inhibitory, and the network toggled between periods of SOM+IN-dominated activity and periods of VIP+IN-dominated activity. The brief periods of SOM+IN activity were accompanied by pauses in network activity, whereas the relatively longer VIP+IN activation periods allowed PYR and PV+INs spiking. Gamma oscillations emerged in the network spiking during periods of VIP+IN activity (Fig. 6A left, 6B left) when PYR and PV+INs interacted to form a type of gamma rhythm known as PING (pyramidal-interneuron network gamma)[91] as observed in the filtered model LFP (Fig. 6B, left). Although theta and alpha oscillations were also apparent, they were not clearly attributable to the spiking activity of any one neuronal subtype.

Using a permutation test similar to the one used to identify significant PAC in the clinical EEG data (Fig. 1), significant LFP PAC was found in the baseline condition between both theta and gamma ($P < 0.01$) as well as between alpha and gamma ($P < 0.05$) (Fig. 6B, left).

We next considered simulations in which VIP+IN excitability was decreased. The overall spiking rate of PYR was greatly reduced (Fig. 6A, right), consistent with findings in mouse models of RTT.[35] The reduction of activity was a consequence of overactivity of SOM+INs, which were released from baseline levels of VIP+IN inhibition, thereby strongly inhibiting all other network components. Although the population spiking of VIP+INs was decreased compared to baseline, gamma still emerged during PING oscillations, which occurred robustly during the brief VIP+IN active periods and sparsely during the periods of SOM+IN overactivity.

Remarkably, despite obvious changes in network dynamics (compared to baseline) when VIP+IN activity was low, the PAC between low frequency (theta and alpha) and high frequency (gamma) oscillations in the model LFP remained statistically significant ($P < 0.05$ in both cases). These results are consistent with our finding of significant theta-gamma and alpha-gamma coupling in the EEG of *both* TD and RTT participants as shown in Fig. 1.

[Insert Figure 6 here]

Figure 6. VIP+ cell hypoactivity alters local network dynamics but PAC remains significant in L4 model. **(A)** Raster plots of simulations of L4 network under conditions of typical VIP+IN activity and when VIP+IN activity is lowered. **(B)** Filtered LFP signals show high (gamma in green) and low (theta in blue and alpha in red) frequency bands and their coordination under typical and low VIP+IN activity conditions. Significant PAC was calculated using a permutation test.

Importantly, if reduction in VIP+IN activity is related to the changes in PAC strength as found in our EEG data, simulations in which VIP+IN activity is lowered should have increased PAC coupling strength compared to the PAC strength under baseline conditions. Therefore, we next investigated if the strength of the gamma modulation by theta and alpha (coupling strength, or MI) changed when VIP+IN activity was lowered. When we compared baseline and low VIP+IN activity conditions, both theta-gamma and alpha-gamma MI were significantly increased in the low VIP+IN condition versus the baseline condition ($P < 0.001$ in both cases) (Fig. 7A), matching the observations in the EEG of RTT participants as shown Figures 2 and 3.

Finally, we probed whether other interneuron subtypes could account for some of the changes to PAC coupling strength seen in the RTT group by repeating the simulation and alternately removing one interneuron subtype at a time. When compared to baseline conditions, removal of SOM+IN activity did not account for increased PAC strength in either theta-gamma or alpha-gamma PAC ($P > 0.05$ in both cases) (Fig. 7B). Removal of PV+IN activity could account for increases in theta-gamma PAC strength ($P < 0.01$) but not alpha-gamma PAC strength ($P > 0.05$). Crucially, only removal of VIP+INs could account for changes to both alpha-gamma and theta-gamma PAC strength. Notably, compared to lowered VIP+IN activity (Fig. 7A), PAC strength increased even more when VIP+IN activity was completely removed (Fig. 7B), indicating that PAC strength may be modulated by the level of VIP+IN deficiency.

[Insert Figure 7 here]

Figure 7. Increased modulation of gamma by slower theta and alpha frequencies with loss of VIP+ cell excitability. (A) Markers represent the modulation index of the theta-gamma or alpha-gamma PAC in the model LFP after 9s of simulation time. Blue markers represent typical VIP+IN activity conditions and red markers represent low VIP+IN activity conditions. $n = 20$ for each group. Difference between groups was calculated using an independent samples t-test, where *** indicates $P < 0.001$. Group mean (horizontal lines) and standard error (vertical lines) are plotted. **(B)** Modulation index of the theta-gamma and alpha-gamma PAC in the model LFP after 9s of simulation time after one interneuron type (SOM+, VIP+ or PV+) was removed from the simulation. An independent samples t-test was used to determine if there was an increase in the mean MI for a particular condition (loss of one type of interneuron) compared to the mean MI in simulations with typical interneuron activity levels (i.e., the "typical VIP+IN activity" level condition), where ** indicates $P < 0.01$ and *** indicates $P < 0.001$.

Overall, our results suggest that RTT-induced VIP+IN deficiency could contribute to the elevated PAC strength observed in RTT.

Discussion

Rett syndrome is a disorder of widespread brain dysfunction, yet its impact on large-scale network activity remains incompletely understood. Oscillatory dynamics—specifically phase–amplitude coupling—offer a powerful, non-invasive window into these disruptions in RTT. With few disease-altering therapeutics currently available, such measures are especially valuable as potential biomarkers that can guide the development and evaluation of targeted interventions.

Here we investigated phase-amplitude coupling in the awake resting state in individuals with RTT compared to typically developing controls. We found that both groups exhibited significant PAC across all electrodes and frequency combinations, confirming widespread cross-frequency coordination at rest, independent of any presence of disorder. However, the RTT group showed more extensive and spatially distributed coupling, particularly in frontal, temporal, and occipital electrodes. PAC strength was significantly elevated in RTT, especially for slower frequencies coupled with low gamma. Analyses of canonical frequency bands further revealed increased theta–gamma PAC strength in posterior, midline, and whole-brain regions, and increased alpha-gamma PAC strength in anterior, posterior, and whole-brain regions. Additionally, alpha–gamma phase bias was shifted toward the falling phase of the low-frequency oscillation in anterior and whole-brain regions. Finally, simulations from a biophysically constrained model showed that reduced excitability in VIP+ interneurons (but not other interneuron subtypes) produced similar elevations in theta-gamma and alpha-gamma PAC strength, supporting a mechanistic link between VIP+IN dysfunction and the empirical data. Together, these findings suggest that PAC captures systems-level abnormalities in neural coordination that may be driven by a particular cell type in RTT.

Elevated theta–gamma coupling in Rett syndrome is notable given the established role of theta-gamma coupling in working memory, episodic encoding, and cognitive control.[23–26] In both humans and animal models, theta phase organizes gamma bursts into discrete representational windows, supporting flexible information integration.[23–26] In the context of RTT, increased theta–gamma coupling may reflect compensatory recruitment of neural resources or inefficient top-down modulation. Alternatively, it could indicate disrupted thalamocortical coordination, a feature implicated in both RTT and other neurodevelopmental conditions.[19,41,56,92] Altered alpha–gamma coupling and phase bias in RTT further implicate disruptions in sensory integration and attentional gating. Alpha rhythms modulate cortical excitability and control sensory gain, while gamma activity reflects local circuit computation[20,93–95]; increased alpha–gamma coupling may therefore reflect a compensatory mechanism aimed at stabilizing sensory processing through enhanced top-down control. The shift in phase bias toward the falling phase of the alpha cycle suggests a disruption in the temporal precision of this gating process. Evaluating PAC metrics in event or task-related paradigms will further clarify the functional role of coupling during active cognitive or sensory engagement.

Disruptions in theta–gamma coupling—characterized by reduced specificity or abnormal timing—have been reported in Fragile X syndrome and ASD,[31,33] while altered alpha-gamma phase bias has been observed in both Phelan-McDermid syndrome[70] and ASD. These findings suggest that aberrant phase-amplitude coupling may reflect shared network-level vulnerabilities across neurodevelopmental disorders, despite divergent genetic etiologies. PAC metrics may

therefore help stratify mechanistically relevant subgroups within heterogeneous conditions like ASD and serve as a systems-level framework for comparing circuit dysfunction across syndromic forms.[31,33]

Despite the robust group differences in PAC between RTT and TD participants, we did not find significant associations between PAC metrics and clinical or phenotypic measures. This may be due to the complexity of the RTT phenotype, which encompasses a broad range of cognitive, motor, sensory, and autonomic dysfunctions. The clinical scales utilized in this study, while valuable for assessing overall disease severity, may not be sufficiently sensitive to detect more subtle cognitive deficits, memory retention, or sensory processing abnormalities that are reflected in PAC dynamics. Developing more specific cognitive and behavioral assessments could help clarify the functional relevance of these neurophysiological findings.

Our computational model of L4 demonstrates that lowered VIP+IN activity may lead to a general reduction of local neural activity along with an increase in the amount of coupling between lower (theta and alpha) and higher (gamma) frequencies. Dysfunction in VIP+INs alone could recapitulate the elevated theta–gamma and alpha–gamma coupling observed in the EEG data, suggesting that lowered VIP+IN activity could contribute to PAC abnormalities in RTT. Our computational results also suggest that VIP+IN deficiency alters network function by increasing SOM+IN modulated inhibitory tone, which restricts signal transmission that would typically occur with higher VIP+IN activity levels. To establish causality between deficiency of VIP and increased theta/gamma and alpha/gamma coupling in RTT, future studies could directly manipulate VIP+IN function in RTT preclinical models. Selective deletion of *Mecp2* from VIP+INs followed by *in vivo* EEG recording would test whether VIP+IN activity is necessary and sufficient to produce elevated PAC. If causality is established between deficiency of VIP+INs and increased theta/gamma and alpha/gamma coupling, future studies can combine experimental event or task-related paradigms with further modeling to identify functional consequences of the altered PAC. Complementary experiments restoring VIP+IN function—either genetically or through targeted neuromodulation—could provide critical insight into reversibility. Notably, non-invasive stimulation approaches that entrain gamma rhythms have been shown to improve pathology via VIP peptide (a peptide co-released with GABA from VIP+INs) in a mouse model of Alzheimer's disease, and may offer a translatable strategy to modulate VIP+IN activity in RTT.[96]

Interestingly, we observed inter-individual variability in PAC strength in the RTT group, with a subset exhibiting MI values similar to TD and a subset exhibiting higher MI. Our model suggests that the elevation in PAC strength may scale with the level of VIP+IN deficiency, and it is possible that some of the heterogeneity observed in the PAC strength of individuals with RTT could be attributable to differing levels VIP+IN dysfunction across individuals or as disease progresses (with greater deficiency of VIP+INs in more severe cases of RTT compared to less severe ones). Most participants in the present study were in the post-regression phase, which may reflect distinct stages of circuit pathology. Longitudinal studies or studies spanning pre- and post-regression ages could help determine whether PAC changes arise early in disease progression or emerge as a consequence of ongoing network changes. Additionally, the type or location of *MECP2* mutations, as well as differential patterns of X chromosome inactivation skewing (on a cell-by-cell and regional basis), influence disease severity[74,97–100] and could thus

impact the nature of PAC alterations and impairment to VIP+INs. Incorporating different disorder stages along with genetic subtype analyses in both preclinical and clinical studies will help clarify inter-individual variability in electrophysiological phenotypes and inform personalized treatment strategies.

Overall, our study identifies altered phase–amplitude coupling as a robust signature of cortical dysfunction in Rett syndrome. By bridging molecular and cellular mechanisms with non-invasive neurophysiological readouts, PAC offers a scalable and clinically accessible tool for tracking circuit-level pathology. Given the widespread use of EEG, PAC could serve not only as a functional biomarker in RTT but also as a generalizable framework for monitoring dysfunction across neurodevelopmental and neuropsychiatric disorders. As our understanding of cell-type-specific contributions to oscillatory dynamics grows, PAC may ultimately help link genetic and cellular pathology to systems-level outcomes and therapeutic response in a broad range of brain disorders.

Data Availability

Data is available upon reasonable request from both NHS and RSBS studies. Code used for modeling will be made available on GitHub.

Author Contributions

DK, AL, and MF conceptualized the study. DK wrote and prepared the initial manuscript draft; YB contributed to the EEG/PAC Methods section. DK, CM, and KS collected clinical data for the RSBS study. DK performed the analysis. YB developed custom analysis scripts. MM provided the main computational contribution. AL, MF, and CN supervised the project. All authors contributed to interpretation of the results and critical revision of the manuscript.

Acknowledgements

Thank you very much to all the participants in these studies and their families, especially those who travelled and extended themselves to contribute to research in Rett syndrome. Thank you to the Rett Syndrome Angels (originally Rett Syndrome Association of Massachusetts) for their incredible support. Thank you to the Rett syndrome clinics and to all members of the labs of Dr.'s April Levin, Michela Fagiolini, Charles Nelson, and Takao Hensch for your invaluable feedback and contributions. This work could not have been completed without all of you.

Funding

This work was supported partially by:
P50HD105351 - Project 1 - Michela Fagiolini
3U54HD061222 - For Rett syndrome, MECP2 Duplications, and Rett-related Disorders Natural History - Alan Percy, Eric Marsh, Tim A. Benke, Jeffrey Neul
P50HD103537 – Jeffrey Neul

Competing interests

Dr. Percy has received research support from the NIH and has been a site PI for Acadia Pharmaceuticals. He is a consultant for Acadia Pharmaceuticals, Taysha Gene Therapies, and Neurogene. He has prepared educational materials for WebMD, Medscape, Pharmacy Times Continuing Education, Prime Inc., and the CME Institute.

References

1. Chahrour M, Zoghbi HY. The Story of Rett Syndrome: From Clinic to Neurobiology. *Neuron*. 2007;56(3):422-437. doi:10.1016/j.neuron.2007.10.001
2. Jeffrey L. Neul, Kaufmann WE, Glaze DG, et al. Rett syndrome: Revised diagnostic criteria and nomenclature. *Ann Neurol*. 2010;68(6):944-950. doi:10.1002/ana.22124
3. Amir RE, Van den Veyver IB, Wan M, Tran CQ, Francke U, Zoghbi HY. Rett syndrome is caused by mutations in X-linked MECP2, encoding methyl-CpG-binding protein 2. *Nat Genet*. 1999;23(2):185-188. doi:10.1038/13810
4. Chen RZ, Akbarian S, Tudor M, Jaenisch R. Deficiency of methyl-CpG binding protein-2 in CNS neurons results in a Rett-like phenotype in mice. *Nat Genet*. 2001;27(3):327-331. doi:10.1038/85906
5. Feldman D, Banerjee A, Sur M. Developmental Dynamics of Rett Syndrome. *Neural Plast*. 2016;2016:1-9. doi:10.1155/2016/6154080
6. Lyst MJ, Bird A. Rett syndrome: a complex disorder with simple roots. *Nat Rev Genet*. 2015;16(5):261-275. doi:10.1038/nrg3897
7. McGraw CM, Samaco RC, Zoghbi HY. Adult Neural Function Requires MeCP2. *Science*. 2011;333(6039):186-186. doi:10.1126/science.1206593
8. Fagiolini M, Patrizi A, LeBlanc J, et al. Intellectual and Developmental Disabilities Research Centers: A Multidisciplinary Approach to Understand the Pathogenesis of Methyl-CpG Binding Protein 2-related Disorders. *Neuroscience*. 2020;445:190-206. doi:10.1016/j.neuroscience.2020.04.037
9. Moser SJ, Weber P, Lütschg J. Rett Syndrome: Clinical and Electrophysiologic Aspects. *Pediatr Neurol*. 2007;36(2):95-100. doi:10.1016/j.pediatrneurol.2006.10.003
10. Buzsáki G, Draguhn A. Neuronal Oscillations in Cortical Networks. *Science*. 2004;304(5679):1926-1929. doi:10.1126/science.1099745
11. Glaze DG. Neurophysiology of Rett syndrome. *Ment Retard Dev Disabil Res Rev*. 2002;8(2):66-71. doi:10.1002/mrdd.10024
12. Niedermeyer E, Rett A, Renner H, et al. Rett syndrome and the electroencephalogram. *Am J Med Genet*. 1986;25(S1):195-199. doi:https://doi.org/10.1002/ajmg.1320250522
13. Tarquinio DC, Hou W, Berg A, et al. Longitudinal course of epilepsy in Rett syndrome and related disorders. *Brain*. 2017;140(2):306-318. doi:10.1093/brain/aww302
14. Roche KJ, LeBlanc JJ, Levin AR, O'Leary HM, Baczewski LM, Nelson CA. Electroencephalographic spectral power as a marker of cortical function and disease severity in girls with Rett syndrome. *J Neurodev Disord*. 2019;11(1):15. doi:10.1186/s11689-019-9275-z
15. Saby JN, Mulcahey PJ, Benke TA, et al. ELECTROENCEPHALOGRAPHIC Correlates of Clinical Severity in the Natural history study of RTT and Related Disorders. *Ann Neurol*. Published online May 9, 2024:ana.26948. doi:10.1002/ana.26948

16. Canolty RT, Knight RT. The functional role of cross-frequency coupling. *Trends Cogn Sci*. 2010;14(11):506-515. doi:10.1016/j.tics.2010.09.001
17. Gips B, Eerden JPJM, Jensen O. A biologically plausible mechanism for neuronal coding organized by the phase of alpha oscillations. Foxe J, ed. *Eur J Neurosci*. 2016;44(4):2147-2161. doi:10.1111/ejn.13318
18. Hyafil A, Giraud AL, Fontolan L, Gutkin B. Neural Cross-Frequency Coupling: Connecting Architectures, Mechanisms, and Functions. *Trends Neurosci*. 2015;38(11):725-740. doi:10.1016/j.tins.2015.09.001
19. Womelsdorf T, Valiante TA, Sahin NT, Miller KJ, Tiesinga P. Dynamic circuit motifs underlying rhythmic gain control, gating and integration. *Nat Neurosci*. 2014;17(8):1031-1039. doi:10.1038/nn.3764
20. Bollimunta A, Mo J, Schroeder CE, Ding M. Neuronal Mechanisms and Attentional Modulation of Corticothalamic Alpha Oscillations. *J Neurosci*. 2011;31(13):4935-4943. doi:10.1523/JNEUROSCI.5580-10.2011
21. Márton CD, Fukushima M, Camalier CR, Schultz SR, Averbeck BB. Signature Patterns for Top-Down and Bottom-Up Information Processing via Cross-Frequency Coupling in Macaque Auditory Cortex. *eneuro*. 2019;6(2):ENEURO.0467-18.2019. doi:10.1523/ENEURO.0467-18.2019
22. Sotero RC, Bortel A, Naaman S, et al. Laminar Distribution of Phase-Amplitude Coupling of Spontaneous Current Sources and Sinks. *Front Neurosci*. 2015;9. doi:10.3389/fnins.2015.00454
23. Holz EM, Glennon M, Prendergast K, Sauseng P. Theta–gamma phase synchronization during memory matching in visual working memory. *NeuroImage*. 2010;52(1):326-335. doi:10.1016/j.neuroimage.2010.04.003
24. Mormann F, Fell J, Axmacher N, et al. Phase/amplitude reset and theta–gamma interaction in the human medial temporal lobe during a continuous word recognition memory task. *Hippocampus*. 2005;15(7):890-900. doi:10.1002/hipo.20117
25. Shirvalkar PR, Rapp PR, Shapiro ML. Bidirectional changes to hippocampal theta–gamma comodulation predict memory for recent spatial episodes. *Proc Natl Acad Sci*. 2010;107(15):7054-7059. doi:10.1073/pnas.0911184107
26. Tort ABL, Komorowski RW, Manns JR, Kopell NJ, Eichenbaum H. Theta–gamma coupling increases during the learning of item–context associations. *Proc Natl Acad Sci*. 2009;106(49):20942-20947. doi:10.1073/pnas.0911331106
27. Seymour RA, Rippon G, Gooding-Williams G, Schoffelen JM, Kessler K. Dysregulated oscillatory connectivity in the visual system in autism spectrum disorder. *Brain*. 2019;142(10):3294-3305. doi:10.1093/brain/awz214
28. Peck F, Naples AJ, Webb SJ, et al. *Phase-Amplitude Coupling in Autism Spectrum Disorder: Results from the Autism Biomarkers Consortium for Clinical Trials*. Neurology; 2022. doi:10.1101/2022.09.25.22279830
29. Gregoriou GG, Gotts SJ, Zhou H, Desimone R. High-Frequency, Long-Range Coupling Between Prefrontal and Visual Cortex During Attention. *Science*. 2009;324(5931):1207-1210. doi:10.1126/science.1171402
30. Khan S, Gramfort A, Shetty NR, et al. Local and long-range functional connectivity is reduced in concert in autism spectrum disorders. *Proc Natl Acad Sci*. 2013;110(8):3107-3112. doi:10.1073/pnas.1214533110

31. Mamashli F, Khan S, Bharadwaj H, et al. Maturational trajectories of local and long□range functional connectivity in autism during face processing. *Hum Brain Mapp*. 2018;39(10):4094-4104. doi:10.1002/hbm.24234
32. Mamashli F, Kozhemiako N, Khan S, et al. Children with autism spectrum disorder show altered functional connectivity and abnormal maturation trajectories in response to inverted faces. *Autism Res*. 2021;14(6):1101-1114. doi:10.1002/aur.2497
33. Radwan B, Dvorak D, Fenton AA. Impaired cognitive discrimination and discoordination of coupled theta–gamma oscillations in Fmr1 knockout mice. *Neurobiol Dis*. 2016;88:125-138. doi:10.1016/j.nbd.2016.01.003
34. Davis P, Takach K, Maski K, Levin A. A circuit-level biomarker of Rett syndrome based on ectopic phase-amplitude coupling during slow-wave-sleep. *Cereb Cortex*. Published online May 31, 2022:bhac226. doi:10.1093/cercor/bhac226
35. Durand S, Patrizi A, Quast KB, et al. NMDA Receptor Regulation Prevents Regression of Visual Cortical Function in the Absence of Mecp2. *Neuron*. 2012;76(6):1078-1090. doi:10.1016/j.neuron.2012.12.004
36. Patrizi A, Awad PN, Chattopadhyaya B, Li C, Di Cristo G, Fagiolini M. Accelerated Hyper-Maturation of Parvalbumin Circuits in the Absence of MeCP2. *Cereb Cortex*. 2020;30(1):256-268. doi:10.1093/cercor/bhz085
37. Dani VS, Chang Q, Maffei A, Turrigiano GG, Jaenisch R, Nelson SB. Reduced cortical activity due to a shift in the balance between excitation and inhibition in a mouse model of Rett Syndrome. *Proc Natl Acad Sci*. 2005;102(35):12560-12565. doi:10.1073/pnas.0506071102
38. He L jie, Liu N, Cheng T lin, et al. Conditional deletion of Mecp2 in parvalbumin-expressing GABAergic cells results in the absence of critical period plasticity. *Nat Commun*. 2014;5(1):5036. doi:10.1038/ncomms6036
39. Ito-Ishida A, Ure K, Chen H, Swann JW, Zoghbi HY. Loss of MeCP2 in Parvalbumin-and Somatostatin-Expressing Neurons in Mice Leads to Distinct Rett Syndrome-like Phenotypes. *Neuron*. 2015;88(4):651-658. doi:10.1016/j.neuron.2015.10.029
40. Mossner JM, Batista-Brito R, Pant R, Cardin JA. Developmental loss of MeCP2 from VIP interneurons impairs cortical function and behavior. *eLife*. 2020;9:e55639. doi:10.7554/eLife.55639
41. Banerjee A, Rikhye RV, Breton-Provencher V, et al. Jointly reduced inhibition and excitation underlies circuit-wide changes in cortical processing in Rett syndrome. *Proc Natl Acad Sci*. 2016;113(46). doi:10.1073/pnas.1615330113
42. Chao HT, Chen H, Samaco RC, et al. Dysfunction in GABA signalling mediates autism-like stereotypies and Rett syndrome phenotypes. *Nature*. 2010;468(7321):263-269. doi:10.1038/nature09582
43. Kullander K, Topolnik L. Cortical disinhibitory circuits: cell types, connectivity and function. *Trends Neurosci*. 2021;44(8):643-657. doi:10.1016/j.tins.2021.04.009
44. Wall NR, De La Parra M, Sorokin JM, Taniguchi H, Huang ZJ, Callaway EM. Brain-Wide Maps of Synaptic Input to Cortical Interneurons. *J Neurosci Off J Soc Neurosci*. 2016;36(14):4000-4009. doi:10.1523/JNEUROSCI.3967-15.2016
45. Batista-Brito R, Vinck M, Ferguson KA, et al. Developmental Dysfunction of VIP Interneurons Impairs Cortical Circuits. *Neuron*. 2017;95(4):884-895.e9. doi:10.1016/j.neuron.2017.07.034

46. Ma G, Liu Y, Wang L, et al. Hierarchy in sensory processing reflected by innervation balance on cortical interneurons. *Sci Adv*. 2021;7(20):eabf5676. doi:10.1126/sciadv.abf5676
47. Mardinly AR, Spiegel I, Patrizi A, et al. Sensory experience regulates cortical inhibition by inducing IGF1 in VIP neurons. *Nature*. 2016;531(7594):371-375. doi:10.1038/nature17187
48. Mesik L, Ma W pei, Li L yun, et al. Functional response properties of VIP-expressing inhibitory neurons in mouse visual and auditory cortex. *Front Neural Circuits*. 2015;9:22. doi:10.3389/fncir.2015.00022
49. Millman DJ, Ocker GK, Caldejon S, et al. VIP interneurons in mouse primary visual cortex selectively enhance responses to weak but specific stimuli. *eLife*. 2020;9:e55130. doi:10.7554/eLife.55130
50. Hakim R, Shamardani K, Adesnik H. A neural circuit for gamma-band coherence across the retinotopic map in mouse visual cortex. *eLife*. 2018;7:e28569. doi:10.7554/eLife.28569
51. Veit J, Handy G, Mossing DP, Doiron B, Adesnik H. Cortical VIP neurons locally control the gain but globally control the coherence of gamma band rhythms. *Neuron*. 2023;111(3):405-417.e5. doi:10.1016/j.neuron.2022.10.036
52. Goff KM, Goldberg EM. Vasoactive intestinal peptide-expressing interneurons are impaired in a mouse model of Dravet syndrome. *eLife*. 2019;8:e46846. doi:10.7554/eLife.46846
53. Rahmatullah N, Schmitt LM, De Stefano L, et al. Hypersensitivity to Distractors in Fragile X Syndrome from Loss of Modulation of Cortical VIP Interneurons. *J Neurosci*. 2023;43(48):8172-8188. doi:10.1523/JNEUROSCI.0571-23.2023
54. Bach S, Shovlin S, Moriarty M, Bardoni B, Tropea D. Rett Syndrome and Fragile X Syndrome: Different Etiology With Common Molecular Dysfunctions. *Front Cell Neurosci*. 2021;15:764761. doi:10.3389/fncel.2021.764761
55. Henriksen MW, Ravn K, Paus B, Von Tetzchner S, Skjeldal OH. De novo mutations in SCN1A are associated with classic Rett syndrome: a case report. *BMC Med Genet*. 2018;19(1):184. doi:10.1186/s12881-018-0700-z
56. Hindriks R, Van Putten MJAM. Thalamo-cortical mechanisms underlying changes in amplitude and frequency of human alpha oscillations. *NeuroImage*. 2013;70:150-163. doi:10.1016/j.neuroimage.2012.12.018
57. Vanneste S, Song JJ, De Ridder D. Thalamocortical dysrhythmia detected by machine learning. *Nat Commun*. 2018;9(1):1103. doi:10.1038/s41467-018-02820-0
58. Bastos G, Holmes JT, Ross JM, et al. Top-down input modulates visual context processing through an interneuron-specific circuit. *Cell Rep*. 2023;42(9):113133. doi:10.1016/j.celrep.2023.113133
59. Chen TW, Li N, Daie K, Svoboda K. A Map of Anticipatory Activity in Mouse Motor Cortex. *Neuron*. 2017;94(4):866-879.e4. doi:10.1016/j.neuron.2017.05.005
60. Whittington MA, Traub RD. Interneuron Diversity series: Inhibitory interneurons and network oscillations in vitro. *Trends Neurosci*. 2003;26(12):676-682. doi:10.1016/j.tins.2003.09.016
61. Scala F, Kobak D, Shan S, et al. Layer 4 of mouse neocortex differs in cell types and circuit organization between sensory areas. *Nat Commun*. 2019;10(1):4174. doi:10.1038/s41467-019-12058-z
62. Börgers C, Epstein S, Kopell NJ. Background gamma rhythmicity and attention in cortical local circuits: A computational study. *Proc Natl Acad Sci*. 2005;102(19):7002-7007. doi:10.1073/pnas.0502366102

63. Wang XJ. Neurophysiological and Computational Principles of Cortical Rhythms in Cognition. *Physiol Rev*. 2010;90(3):1195-1268. doi:10.1152/physrev.00035.2008
64. Chartove JAK, McCarthy MM, Pittman-Polletta BR, Kopell NJ. A biophysical model of striatal microcircuits suggests gamma and beta oscillations interleaved at delta/theta frequencies mediate periodicity in motor control. Migliore M, ed. *PLOS Comput Biol*. 2020;16(2):e1007300. doi:10.1371/journal.pcbi.1007300
65. Percy AK, Benke TA, Marsh ED, Neul JL. Rett syndrome: The Natural History Study journey. *Ann Child Neurol Soc*. 2024;2(3):189-205. doi:10.1002/cns3.20086
66. Levin AR, Méndez Leal AS, Gabard-Durnam LJ, O'Leary HM. BEAPP: The Batch Electroencephalography Automated Processing Platform. *Front Neurosci*. 2018;12:513. doi:10.3389/fnins.2018.00513
67. Gabard-Durnam LJ, Mendez Leal AS, Wilkinson CL, Levin AR. The Harvard Automated Processing Pipeline for Electroencephalography (HAPPE): Standardized Processing Software for Developmental and High-Artifact Data. *Front Neurosci*. 2018;12:97. doi:10.3389/fnins.2018.00097
68. Winkler I, Haufe S, Tangermann M. Automatic Classification of Artifactual ICA-Components for Artifact Removal in EEG Signals. *Behav Brain Funct*. 2011;7(1):30. doi:10.1186/1744-9081-7-30
69. Winkler I, Brandl S, Horn F, Waldburger E, Allefeld C, Tangermann M. Robust artifactual independent component classification for BCI practitioners. *J Neural Eng*. 2014;11(3):035013. doi:10.1088/1741-2560/11/3/035013
70. Mariscal MichaelG, Berry-Kravis E, Buxbaum JD, et al. Shifted phase of EEG cross-frequency coupling in individuals with Phelan-McDermid syndrome. *Mol Autism*. 2021;12(1):29. doi:10.1186/s13229-020-00411-9
71. Berman JI, Liu S, Bloy L, Blaskey L, Roberts TPL, Edgar JC. Alpha-to-Gamma Phase-Amplitude Coupling Methods and Application to Autism Spectrum Disorder. *Brain Connect*. 2015;5(2):80-90. doi:10.1089/brain.2014.0242
72. Dupré La Tour T, Tallot L, Grabot L, et al. Non-linear auto-regressive models for cross-frequency coupling in neural time series. Battaglia FP, ed. *PLOS Comput Biol*. 2017;13(12):e1005893. doi:10.1371/journal.pcbi.1005893
73. Tort ABL, Komorowski R, Eichenbaum H, Kopell N. Measuring Phase-Amplitude Coupling Between Neuronal Oscillations of Different Frequencies. *J Neurophysiol*. 2010;104(2):1195-1210. doi:10.1152/jn.00106.2010
74. Neul JL, Fang P, Barrish J, et al. Specific mutations in Methyl-CpG-Binding Protein 2 confer different severity in Rett syndrome. *Neurology*. 2008;70(16):1313-1321. doi:10.1212/01.wnl.0000291011.54508.aa
75. Guy W. Clinical global impressions. In: Guy W, editor. ECDEU assessment manual for psychopharmacology (Revised) National Institute of Mental Health; Rockville, Maryland: 1976. pp. 217–221.
76. Neul JL, Glaze DG, Percy AK, et al. Improving Treatment Trial Outcomes for Rett Syndrome: The Development of Rett-specific Anchors for the Clinical Global Impression Scale. *J Child Neurol*. 2015;30(13):1743-1748. doi:10.1177/0883073815579707
77. Mount RH, Charman T, Hastings RP, Reilly S, Cass H. The Rett Syndrome Behaviour Questionnaire (RSBQ): refining the behavioural phenotype of Rett syndrome. *J Child Psychol Psychiatry*. 2002;43(8):1099-1110. doi:10.1111/1469-7610.00236

78. Percy AK, Neul JL, Benke TA, Marsh ED, Glaze DG. A review of the Rett Syndrome Behaviour Questionnaire and its utilization in the assessment of symptoms associated with Rett syndrome. *Front Pediatr*. 2023;11:1229553. doi:10.3389/fped.2023.1229553
79. Oberman LM, Leonard H, Downs J, et al. Rett Syndrome Behaviour Questionnaire in Children and Adults With Rett Syndrome: Psychometric Characterization and Revised Factor Structure. *Am J Intellect Dev Disabil*. 2023;128(3):237-253. doi:10.1352/1944-7558-128.3.237
80. Dunn, W. Sensory Profile 2. NCS Pearson, Inc., 2014.
81. Tomchek SD, Dunn W. Sensory Processing in Children With and Without Autism: A Comparative Study Using the Short Sensory Profile. *Am J Occup Ther*. 2007;61(2):190-200. doi:10.5014/ajot.61.2.190
82. Wang SY, Lee WT, Shieh JY, et al. Multidimensional Development and Adaptive Behavioral Functioning in Younger and Older Children With Rett Syndrome. *Phys Ther*. 2022;102(4). doi:10.1093/ptj/pzab297
83. Sparrow SS, Cicchetti DV, Saulnier CA. Vineland Adaptive Behavior Scales, Third Edition (Vineland-3): Manual. Bloomington, MN: Pearson Assessments; 2016.
84. Barnes KV, Coughlin FR, O'Leary HM, et al. Anxiety-like behavior in Rett syndrome: characteristics and assessment by anxiety scales. *J Neurodev Disord*. 2015;7(1). doi:10.1186/s11689-015-9127-4
85. Esbensen AJ, Rojahn J, Aman MG, Ruedrich S. Reliability and Validity of an Assessment Instrument for Anxiety, Depression, and Mood Among Individuals with Mental Retardation. *J Autism Dev Disord*. 2003;33(6):617-629. doi:10.1023/b:jadd.0000005999.27178.55
86. Rudy B, Fishell G, Lee S, Hjerling□Leffler J. Three groups of interneurons account for nearly 100% of neocortical GABAergic neurons. *Dev Neurobiol*. 2011;71(1):45-61. doi:10.1002/dneu.20853
87. Ma Y, Hu H, Berrebi AS, Mathers PH, Agmon A. Distinct Subtypes of Somatostatin-Containing Neocortical Interneurons Revealed in Transgenic Mice. *J Neurosci*. 2006;26(19):5069-5082. doi:10.1523/JNEUROSCI.0661-06.2006
88. Olufsen MS, Whittington MA, Camperi M, Kopell N. New roles for the gamma rhythm: population tuning and preprocessing for the Beta rhythm. *J Comput Neurosci*. 2003;14(1):33-54. doi:10.1023/A:1021124317706
89. Adam E, Kowalski M, Akeju O, et al. Ketamine can produce oscillatory dynamics by engaging mechanisms dependent on the kinetics of NMDA receptors. *Proc Natl Acad Sci*. 2024;121(22). doi:10.1073/pnas.2402732121
90. Kramer MA, Eden UT. *Case Studies in Neural Data Analysis: A Guide for the Practicing Neuroscientist*. The MIT Press; 2016.
91. Whittington MA, Cunningham MO, LeBeau FEN, Racca C, Traub RD. Multiple origins of the cortical gamma rhythm. *Dev Neurobiol*. 2011;71(1):92-106. doi:10.1002/dneu.20814
92. Tzeng CP, Whitwam T, Boxer LD, et al. Activity-induced MeCP2 phosphorylation regulates retinogeniculate synapse refinement. *Proc Natl Acad Sci*. 2023;120(44):e2310344120. doi:10.1073/pnas.2310344120
93. Buzsáki G, Wang XJ. Mechanisms of Gamma Oscillations. *Annu Rev Neurosci*. 2012;35(1):203-225. doi:10.1146/annurev-neuro-062111-150444
94. Jensen O, Mazaheri A. Shaping Functional Architecture by Oscillatory Alpha Activity: Gating by Inhibition. *Front Hum Neurosci*. 2010;4. doi:10.3389/fnhum.2010.00186

95. Cardin JA. Snapshots of the Brain in Action: Local Circuit Operations through the Lens of γ Oscillations. *J Neurosci*. 2016;36(41):10496-10504. doi:10.1523/JNEUROSCI.1021-16.2016
96. Murdock MH, Yang CY, Sun N, et al. Multisensory gamma stimulation promotes glymphatic clearance of amyloid. *Nature*. 2024;627(8002):149-156. doi:10.1038/s41586-024-07132-6
97. Cuddapah VA, Pillai RB, Shekar KV, et al. *Methyl-CpG-binding protein 2* (*MECP2*) mutation type is associated with disease severity in Rett syndrome. *J Med Genet*. 2014;51(3):152-158. doi:10.1136/jmedgenet-2013-102113
98. Frullanti E, Papa FT, Grillo E, et al. Analysis of the Phenotypes in the Rett Networked Database. *Int J Genomics*. 2019;2019:1-9. doi:10.1155/2019/6956934
99. Bebbington A, Anderson A, Ravine D, et al. Investigating genotype-phenotype relationships in Rett syndrome using an international data set. *Neurology*. 2008;70(11):868-875. doi:10.1212/01.wnl.0000304752.50773.ec
100. Merritt JK, Fang X, Caylor RC, et al. Normalized Clinical Severity Scores Reveal a Correlation between X Chromosome Inactivation and Disease Severity in Rett Syndrome. *Genes*. 2024;15(5):594. doi:10.3390/genes15050594

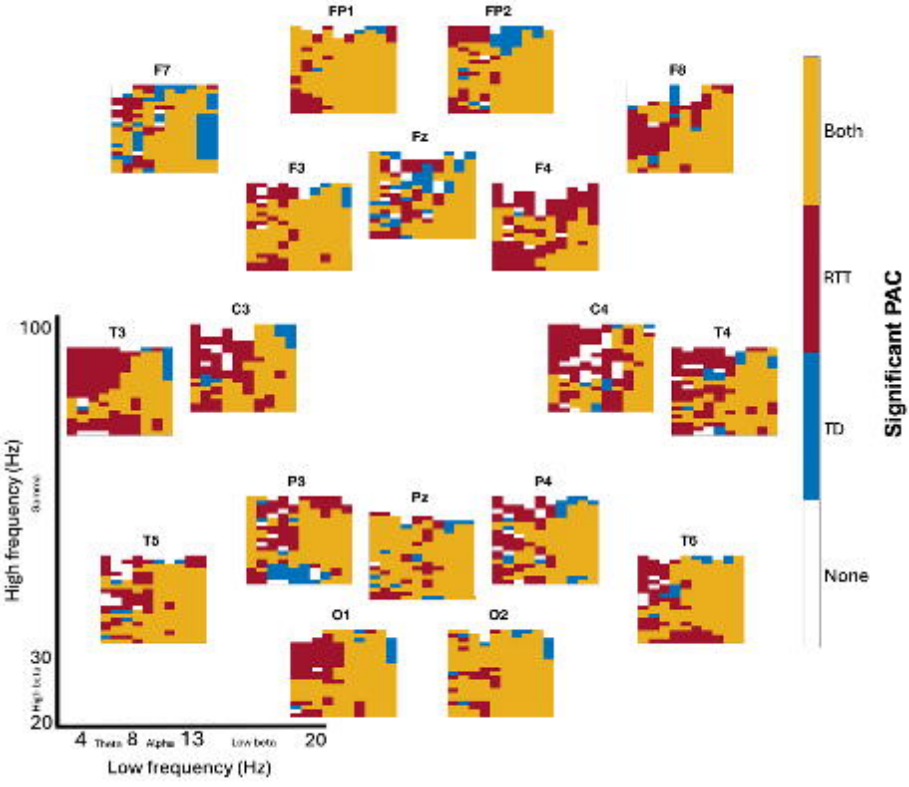
FP1
FP2
F7
F8
Fz
F3
F4
C3
C4
T3
T4
P3
Pz
P4
T5
T6
O1
O2
Both
RTT
TD
None
Significant PAC
100
30
20
High frequency (Hz)
4
8
13
20
Low frequency (Hz)

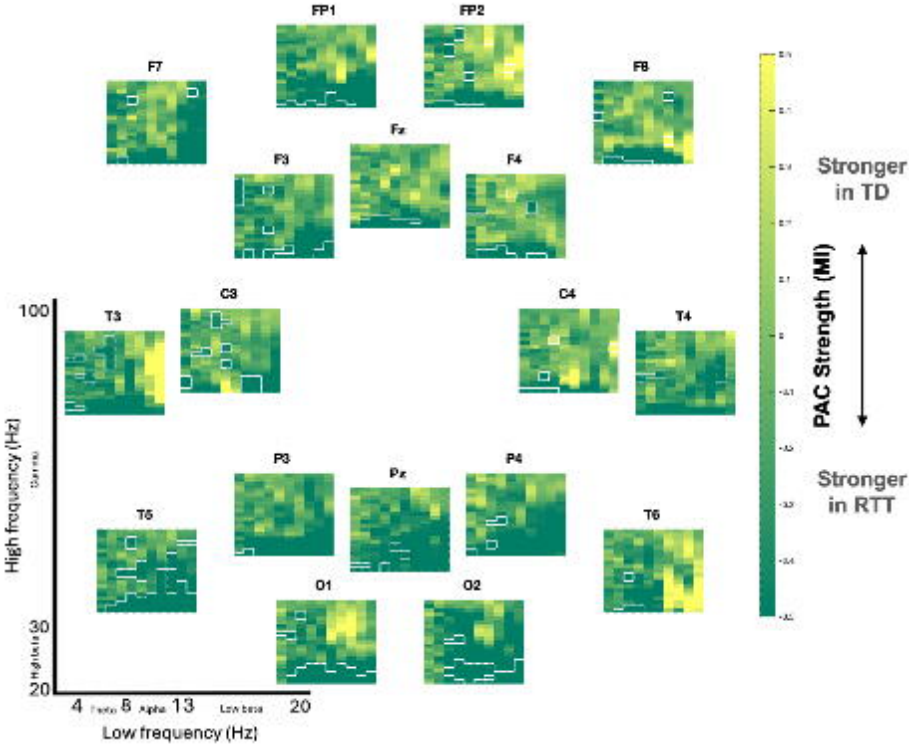
FP1
FP2
F7
F8
Fz
F3
F4
C3
C4
T3
T4
P3
Pz
P4
T5
T6
O1
O2
100
30
20
4
8
13
20
High frequency (Hz)
Low frequency (Hz)
Alpha
Stronger in TD
PAC Strength (MI)
Stronger in RTT

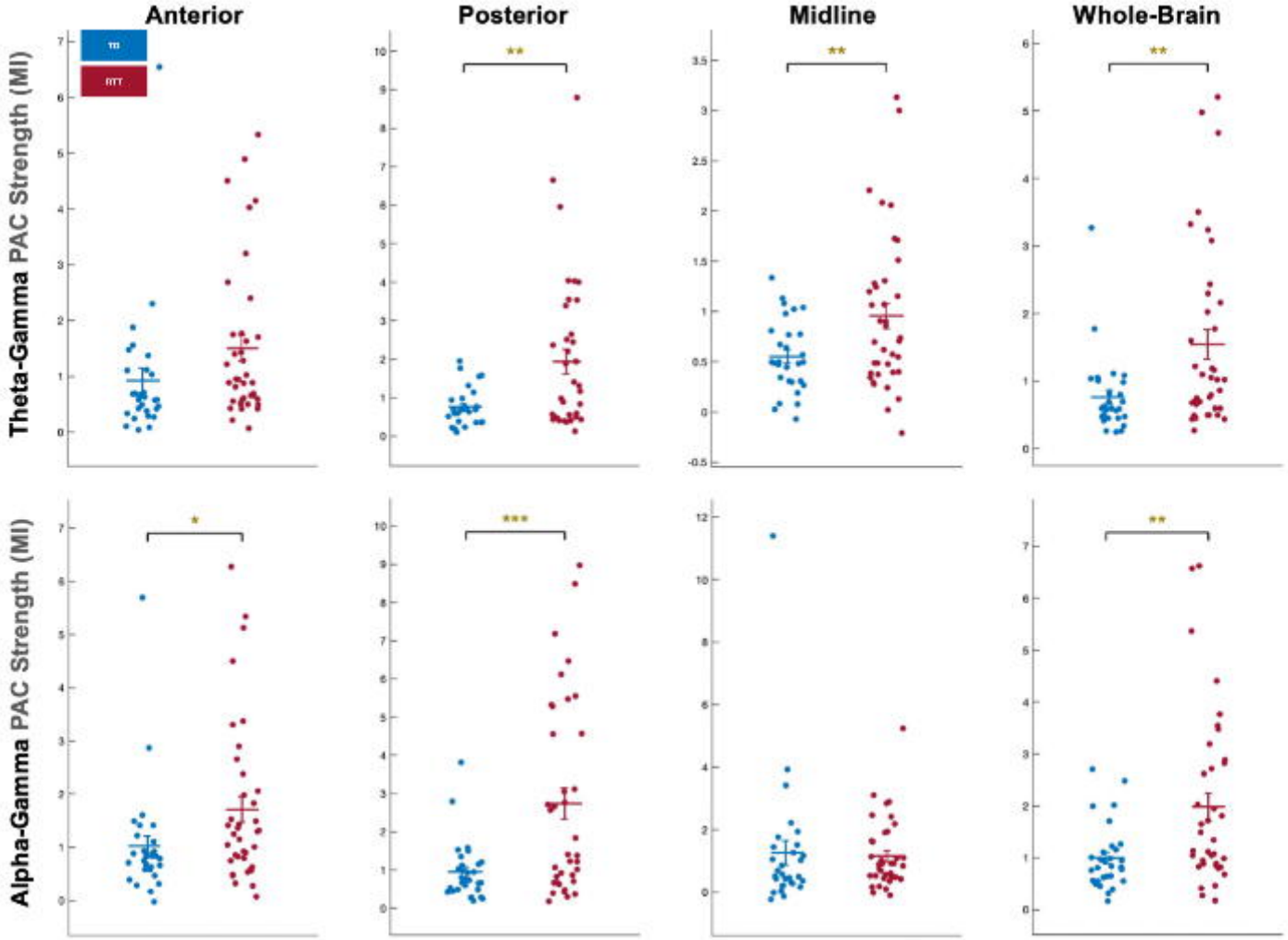
Anterior
Posterior
Midline
Whole-Brain
TD
RTT
Theta-Gamma PAC Strength (MI)
Alpha-Gamma PAC Strength (MI)
*
**
***

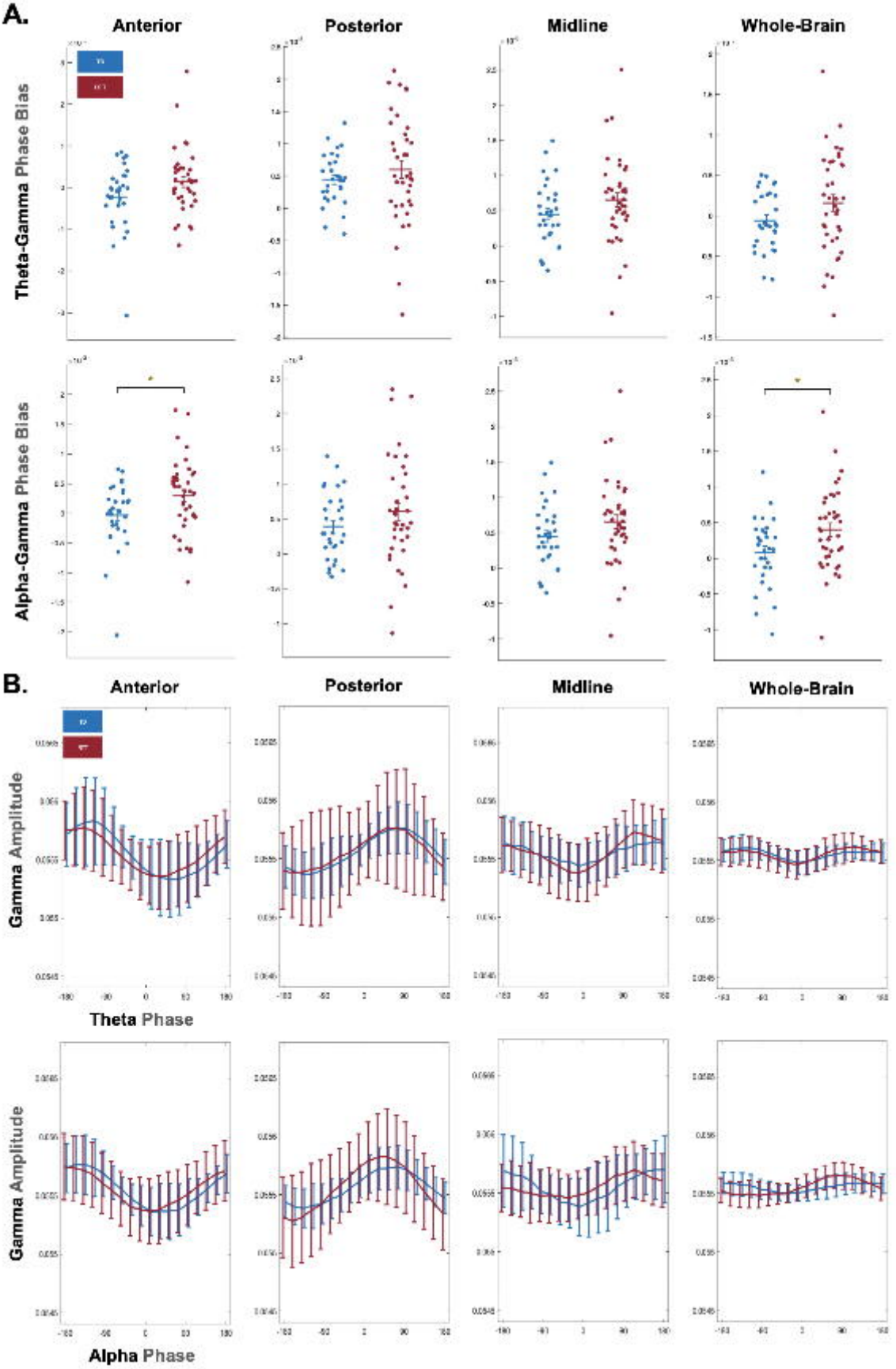
A.
Anterior
Posterior
Midline
Whole-Brain
Theta-Gamma Phase Bias
Alpha-Gamma Phase Bias
B.
Anterior
Posterior
Midline
Whole-Brain
Gamma Amplitude
Theta Phase
Gamma Amplitude
Alpha Phase

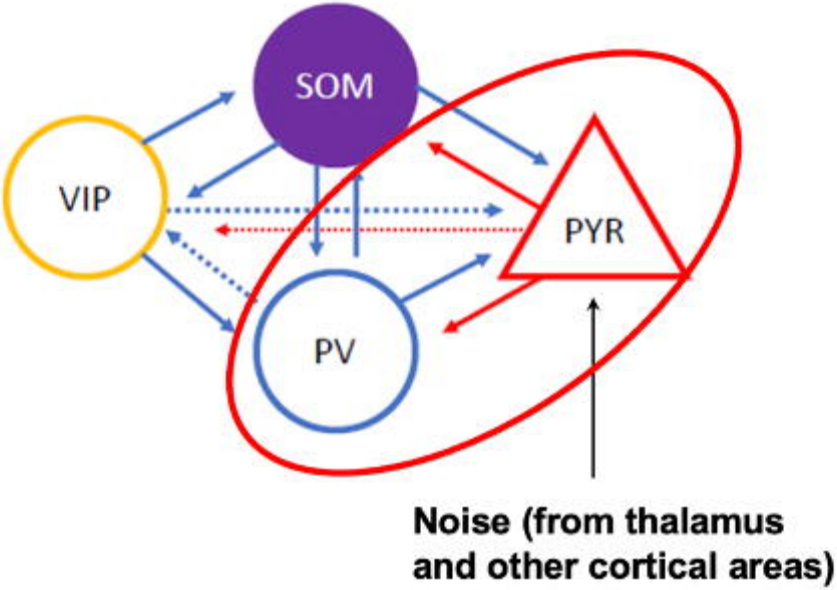
SOM
VIP
PYR
PV
Noise (from thalamus
and other cortical areas)

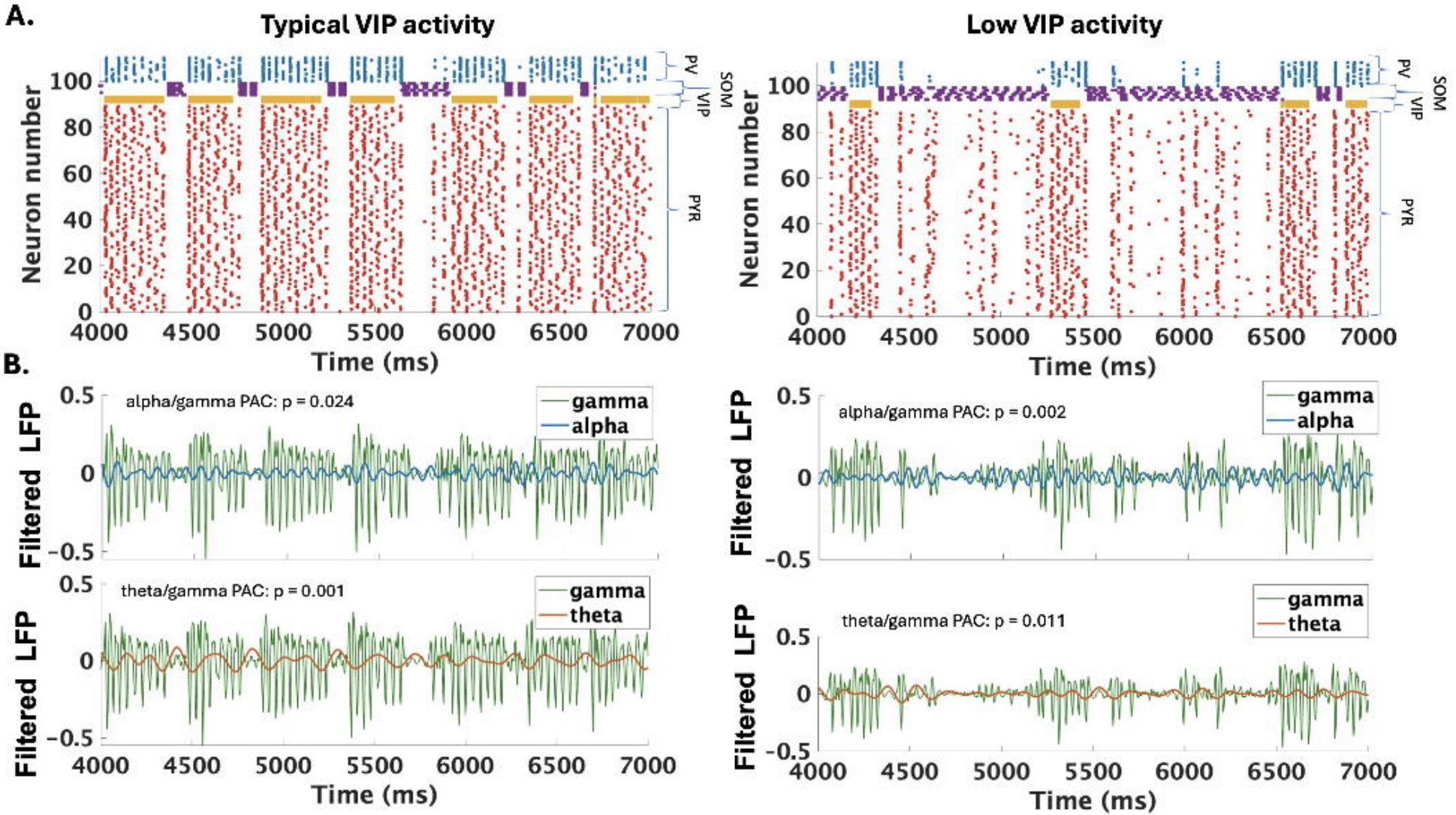
A.
Typical VIP activity
Low VIP activity
Neuron number
Time (ms)
PV
SOM
VIP
PYR
B.
alpha/gamma PAC: p = 0.024
alpha/gamma PAC: p = 0.002
theta/gamma PAC: p = 0.001
theta/gamma PAC: p = 0.011
gamma
alpha
theta
Filtered LFP

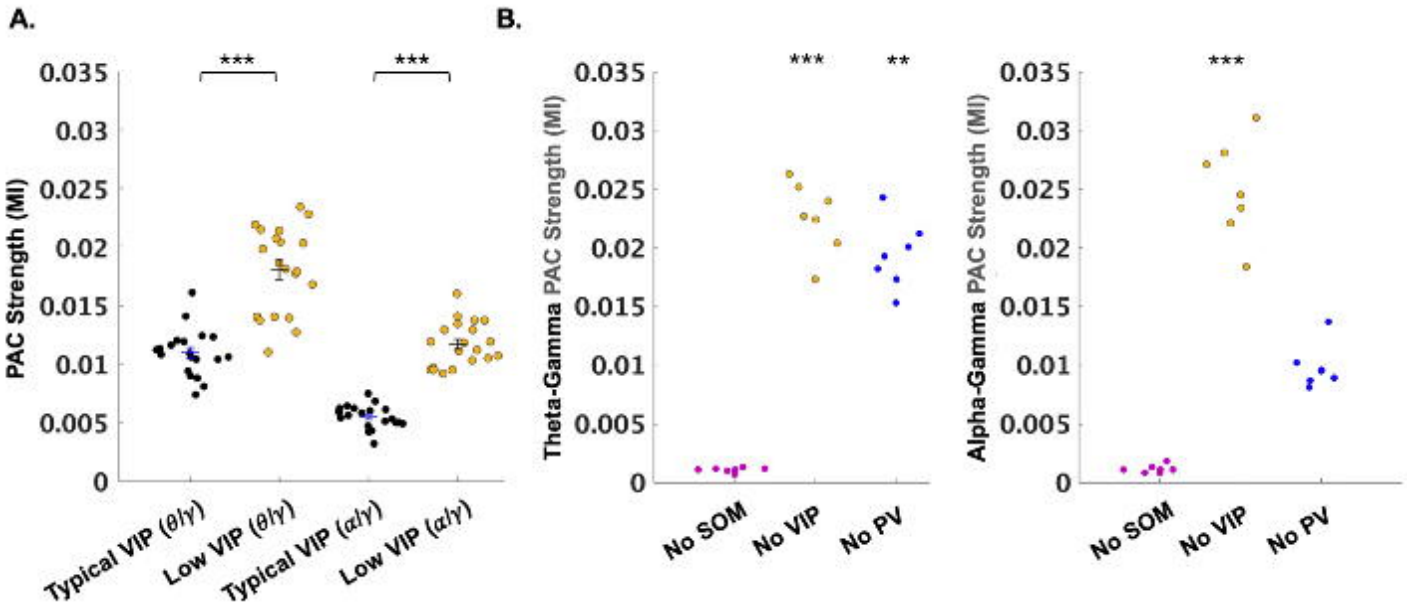
A.
B.
PAC Strength (MI)
0.035
0.03
0.025
0.02
0.015
0.01
0.005
0
***
***
Typical VIP (θ/γ)
Low VIP (θ/γ)
Typical VIP (α/γ)
Low VIP (α/γ)
Theta-Gamma PAC Strength (MI)
***
**
No SOM
No VIP
No PV
Alpha-Gamma PAC Strength (MI)
***
No SOM
No VIP
No PV